Infrared Interferometric observation of dust in the nuclei of active galaxies

Raban, D.

Chapter 3

Resolving the dusty torus in NGC 1068

Abstract. We present new interferometric data obtained with MIDI (MID infrared Interferometric instrument) for the Seyfert II galaxy NGC 1068, with an extensive coverage of sixteen *uv* points. These observations resolve the nuclear mid-infrared emission from NGC 1068 in unprecedented detail with a maximum resolution of 7 milliarcseconds.
For the first time, sufficient *uv* points have been obtained, allowing us to generate an image of the source using maximum entropy image reconstruction. The features of the image are similar to those obtained by modelling.
We find that the mid-infrared emission can be represented by two components, each with a Gaussian brightness distribution. The first, identified as the inner funnel of the obscuring torus, is hot (∼800K), 1.35 parsec long, and 0.45 parsec thick in FWHM at a PA=-42° (from north to east). It has an absorption profile different than standard interstellar dust and with evidence for clumpiness.
The second component is 3×4 pc in FWHM with T=∼300K, and we identify it with the cooler body of the torus. The compact component is tilted by $\sim 45^\circ$ with respect to the radio jet and has similar size and orientation to the observed water maser distribution.
We show how the dust distribution relates to other observables within a few parsecs of the core of the galaxy such as the nuclear masers, the radio jet, and the ionization cone. We compare our findings to a similar study of the Circinus galaxy and other relevant studies.
Our findings shed new light on the relation between the different parsec-scale components in NGC 1068 and the obscuring torus.

D. Raban, W. Jaffe, H. Röttgering, K. Meisenheimer and K. Tristram
Monthly Notices of the Roayal Astronomical Society, 394, 1325 (2009)

3.1 Introduction

THE AGN unification model (Antonucci 1993; Urry & Padovani 1995) explains the difference between type II Seyferts, which show only narrow emission lines, and type I, which show both narrow and broad emission lines, by stipulating that a torus-like structure surrounds the central engine and accretion disk. Thus, when oriented edge-on, the torus blocks the subparsec-sized broad emission line region making the object appear as a type II, while harbouring an unseen type I nucleus. Symmetry and angular momentum considerations suggest that the torus and the accretion disk are perpendicular to the bipolar jet, whose orientation is likely to be coupled closely to that of the accreted matter. The relative number of Seyfert I/II demands that the torus be geometrically thick (Osterbrock & Shaw 1988), although thick structures orbiting compact objects will quickly lose their height and collapse into a thin disk. In order to maintain its stable torus structure, the random velocities of the dust clouds need to be of an order similar to the orbital speed, or a few hundred km/s. Since colliding dust clouds are destroyed at relative speeds as low as a few meters per second, the dust clouds are not expected to last very long (Krolik & Begelman 1988). To overcome the difficulty of maintaining its inflated state different dust configuration other than a torus have been introduced, such as the warped disk of Sanders et al. (1989). Alternatively, the dust has been described as a hydrodynamically driven outflow (Kartje & Königl 1996).

NGC 1068 is considered to be the prototype Seyfert II galaxy, where the central source is obscured by dust. Its relatively small distance of 14.4 Mpc and high mid-infrared flux make the object ideally suited for the study of the nucleus and obscuring dust. Previous MIDI observations of NGC 1068 revealed warm (320 K) silicate dust in a structure 2.1 parsecs thick and 3.4 parsecs in diameter, surrounding a small, hot (800K) component whose shape and orientation could not be determined in detail (Jaffe et al. 2004) (hereafter J04). These observations were, together with those of Wittkowski et al. (2004) (W04), the first to spatially resolve direct emission from the putative torus, and the first to show that a torus-like structure is indeed present in NGC 1068.

The mid-infrared emission from the central region of NGC 1068, as seen by the largest single dish telescopes, is composed of an unresolved core plus extended emission. Deconvolved maps at 12μm taken with VISIR (Imager and Spectrometer in the InfraRed at the Very Large Telescope) by Galliano et al. (2005) reveal a set of discrete mid-infrared sources: seven in the north-eastern quadrant and five in the south-eastern quadrant. The central source, observed with the 10m Keck telescope (Bock et al. 2000), is extended by $\sim$1" in the north-south direction and is unresolved in the east-west direction. About 2/3 of its flux can be ascribed to a core structure which is itself elongated north-south in a tongue-shaped structure and according to Bock et al. (2000) does not show a distinct unresolved core. Recent 12.8μm speckle images taken with VISIR in BURST mode by Poncelet et al. (2007) identify two major sources of emission at 12.8μm: a compact source (< 85 mas) and an elliptical source of size (< 140) mas $\times$ 1187 mas and PA$\sim 4^\circ$. It is the unresolved compact source which is associated with the dusty torus and is the subject of this study. Other parsec scale components in NGC 1068 that are related to the torus are the compact H_2O masers , appearing on

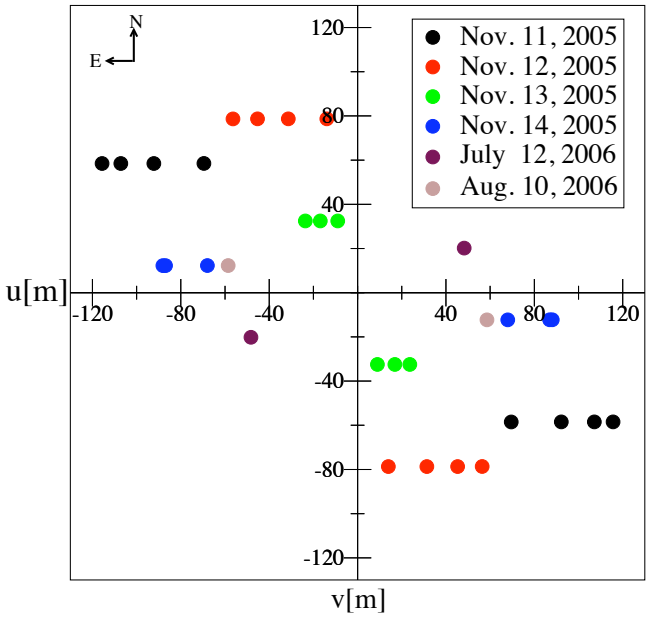

Figure 3.1 — *uv* coverage [m] for NGC1068 and colour coded by date. Due to the ∼0.0 declination of NGC1068, the *uv* tracks are parallel to the u-axis. *uv* coords [u,v] are complex conjugates of uv coords [-u,-v], and both are plotted since they are indistinguishable.

the sky as a set of linear spots (PA=$-45°$) that are misaligned with the jet and span a velocity range of 600 km/s with a sub-Keplerian velocity profile ($v \propto r^{-0.3}$). The kinematics of the maser spots indicate that the masers are located in a rotating disk with inner radius of ∼0.65 pc and outer radius of ∼1.1 pc (Gallimore et al. 2001). This disk traces the outer, colder part of the accretion disk where conditions allow for the formation of water masers. It was proposed earlier that these masers trace warm molecular dust (Claussen & Lo 1986), a conclusion supported by the observations presented here which reveal the dusty torus to be at the outer edge of the maser disk. VLBA 5 and 8.4GHz radio continuum images show a parsec-sized structure with a major axis at PA≃-75°, most likely indicating free-free emission from hot (T=$10^4 - 10^5$ K) ionized gas (Gallimore et al. 2004). According to the unification model, toroidal obscuration by dust is also responsible for the conical shape of the narrow-line region. The ionization cone in NGC 1068 as seen in HST images is centred around PA=$10°$, while modelling of HST spectra, based on the kinematics of the gas indicate the ionization cone with an opening angle of $80°$ centred around PA=$30°$ (Das et al. 2006), roughly perpendicular to the maser spots.

3.2 Observations, *uv* coverage and data reduction

MIDI is the mid-infrared interferometer located on Cerro Paranal in northern Chile and operated by the European Southern Observatory (ESO). MIDI functions as a classical Michelson interferometer, combining the light from two 8-meter unit telescopes (UTs). For a detailed description of the instrument see Leinert et al. (2003). The main data product of MIDI is the correlated flux, which can be explained as the spectrum of the source at a certain spatial resolution projected perpendicular to the baseline, that is to the projected separation of the two telescopes.

A total of 16 interferometric observations were taken together with a single-dish total flux spectrum for each one. Table 3.1 contains the observation log. All observations

Table 3.1. Log of the observations dates, unit telescopes used and baseline configuration in polar (D[m], PA[degree]) coordinates projected on sky.

No.	Date	# UT's	D	PA	resolution[a]
#1	Nov. 11, 2005	UT1-UT4	90.8	50.0	10.3
#2		″	109.2	57.6	8.6
#3		″	122.	61.4	7.7
#4		″	129.6	63.2	7.2
#5	Nov. 12, 2005	UT1-UT3	79.9	10.0	11.7
#6		″	84.7	21.7	11
#7		″	90.8	29.9	10.3
#8		″	96.8	35.6	9.7
#9	Nov. 13, 2005	UT2-UT3	33.6	15.5	27.9
#10		″	36.6	27.5	25.6
#11		″	40.15	36.1	23.4
#12	Nov. 14, 2005	UT2-UT4	69.0	79.8	13.6
#13		″	89.98	82.1	10.4
#14		″	87.76	82.0	10.7
#15	July 12, 2006	UT3-UT4	52.3	-67.3	17.9
#16	Aug. 10, 2006	UT2-UT4	59.82	78.2	15.6

[a]The spatial resolution in milliarseconds is calculated by $\theta = \lambda/(2.2B)$ where B is the projected baseline separation and $\lambda = 10\mu m$.

were done in GRISM mode with a spectral resolution of $\lambda/\Delta\lambda = 230$. The same calibrator, HD10380, was used for all observations with identical settings. Chopping with $f = 1$Hz, and throw amplitude of 15″ at an angle $\alpha = 0^\circ$ was applied during photometric measurement and acquisition. Fringes were tracked in "offset tracking" mode.

A map of the *uv* coverage is shown in Fig. 3.1. Due to the near zero declination of NGC 1068 the tracks are parallel to the u-axis, causing each observation to differ both by baseline length and position angle from its neighbours. The distribution of the tracks is concentrated in the second/fourth quarter of the *uv* plane, with only one observation on a perpendicular baseline, reflecting the fixed physical placement of the VLTI unit telescopes. After each interferometric observation, a total flux measurement (i.e. single-dish spectrum) is taken from each telescope independently, and used to determine the visibility, i.e. the correlated interferometric flux divided by the geometric mean of the single dish fluxes. Only one such observation was rejected due to bad seeing, and the remaining 15 fluxes were averaged together (Fig. 3.2). A typical MIDI observation is recorded in 8000 frames, with an integration time of 0.036 seconds for each frame. We examined the total flux recorded on the detector per frame, and rejected frames where the flux was unstable. Data reduction was done by coherent vis-

ibility estimation with the Expert Work Station (EWS) package written in Leiden. See Jaffe (2004) for a detailed description of the coherent visibility estimation method.

3.2.1 Calibration

Calibration of the interferometric and photometric data was done using HD10380 as the calibrator star for all observations. Each night's observation started with HD10380, and it was observed between observations of NGC 1068. Thus, we obtained a calibration measurement for each *uv* point of NGC 1068. The calibrator's data reduction was done using the same parameters as for NGC 1068 and went through the same tests for consistency as for the science target. Only one calibrator observation was rejected due to bad seeing. Calibration measurements taken just before and after NGC 1068 were compared and, if different, were averaged. For an unresolved point source, the correlated flux should equal the total flux. Assuming this, we can calibrate the correlated fluxes using the calibrators, without a need to use the photometry measurements, which are less reliable due to the strong atmospheric background. The calibrated fluxes are computed by dividing the correlated fluxes of the target by those of the calibrator, and then multiplying by the known flux of the calibrator. For HD 10380 we used the spectral template of Cohen et al. (1999). The calibrated photometric fluxes were produced by the same procedure for the photometric data.

3.2.2 Correlated flux. vs. visibility

Optical/infrared interferometric data is often presented as visibility data, a dimensionless quantity, which measures the fraction of flux that is resolved for a given baseline. Here we prefer to use the correlated fluxes, the actual flux that the interferometer measures for a given baseline, as is common practice in radio interferometry. Determining the visibility, V, directly from the contrast of the interferometric fringes ($V = (I_{max} - I_{min})/(I_{max} + I_{min})$) is not practical since the amount of flux reaching the beam combiner from the two telescopes is generally not equal and therefore affects the contrast of the fringes. Given an isolated source, the visibilities equal the correlated fluxes divided by the total flux of the source. If, however, the source is embedded in emission on larger scales (as seems to be the case for NGC 1068), then the total flux determined by a larger field of view is contaminated by the large scale emission making it difficult to interpret. The correlated fluxes also free us from handling the strong atmospheric background, which is not correlated and is removed easily in the data reduction process.

3.3 Results

3.3.1 The total flux

The total flux of NGC 1068 is shown in Fig. 3.2, as measured by the average of two 8-meter UTs, each with a beam size of 250 mas . It is in rough agreement with previously published spectra from 8m class telescopes. The only spectral feature seen in the total flux is the 9.7μm silicate feature, in absorption. We do not detect the very weak [SIV] emission line reported by Rhee & Larkin (2006) and Mason et al. (2006) with similar

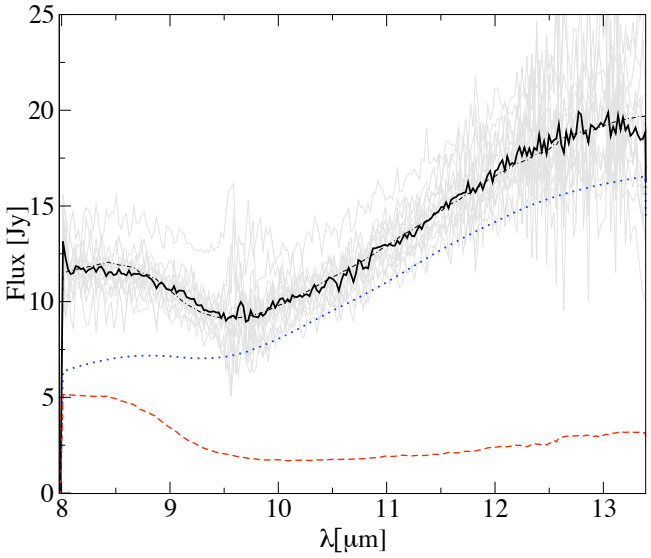

Figure 3.2 — Total (single-dish) flux. All 15 individual spectra are in grey with the mean given in black. The dash-dotted line is the model fit described in section 3.4.1, which is composed of two flux components: component 1 (red-dashed) and component 2 (blue-dotted). Note the atmospheric O_3 feature at 9.7μm.

apertures. Space based instruments show PAH features at $\lambda = 7.6, 9$ and 10.9μm (Sturm et al. 2000). These features are found to occur at larger distances from the nucleus.

3.3.2 The correlated (interferometric) fluxes

The correlated fluxes, shown in Figures 3.3&3.4 display large variations in the shape and depth of the silicate feature centred at 9.7μm, the only spectral feature present in the data. No traces of PAH molecules or the 12.9μm Ne line are seen. The clear relation seen in the data between the baseline length and the correlated flux shows that the source is resolved on every baseline. The 'bump' around 9.7μm seen in baselines #9-14,16 (Figures 3.3&3.4) is due to the atmospheric ozone feature, centred 9.7μm.

3.3.3 Discussion of the results

The correlated fluxes in fact sample the SED of NGC 1068 about a range of different orientations and spatial resolutions. The structure of the spectra, and in particular the 9.7μm silicate feature, varies considerably with baselines, and is quite different from the total flux. The striking differences between the correlated and total fluxes demonstrate how inadequate the total flux is as the sole means to constrain torus models. Indeed, numerous authors have attempted to fit tori models to the SED of NGC 1068, and many different models fit the SED equally well, as was first demonstrated by Galliano et al. (2003).

The depth of the silicate feature in the correlated fluxes is about 0.6 of the continuum level (as defined by the average of the flux at 8 and 13μm) and is independent of baseline length. This suggests that the emitting medium is compact and is located in a region much smaller than the absorbing medium. For the total flux, the silicate feature depth is smaller, ~ 0.3. The total flux can be successfully fitted with a combination of two grey body spectra, a warm (~300K) component, plus a hot (~800K) compact component, both behind uniform absorption screens as discussed in §3.4.1. In general we find the total flux to be easily reproducible by our models described in §3.4.1 for a wide range of parameters.

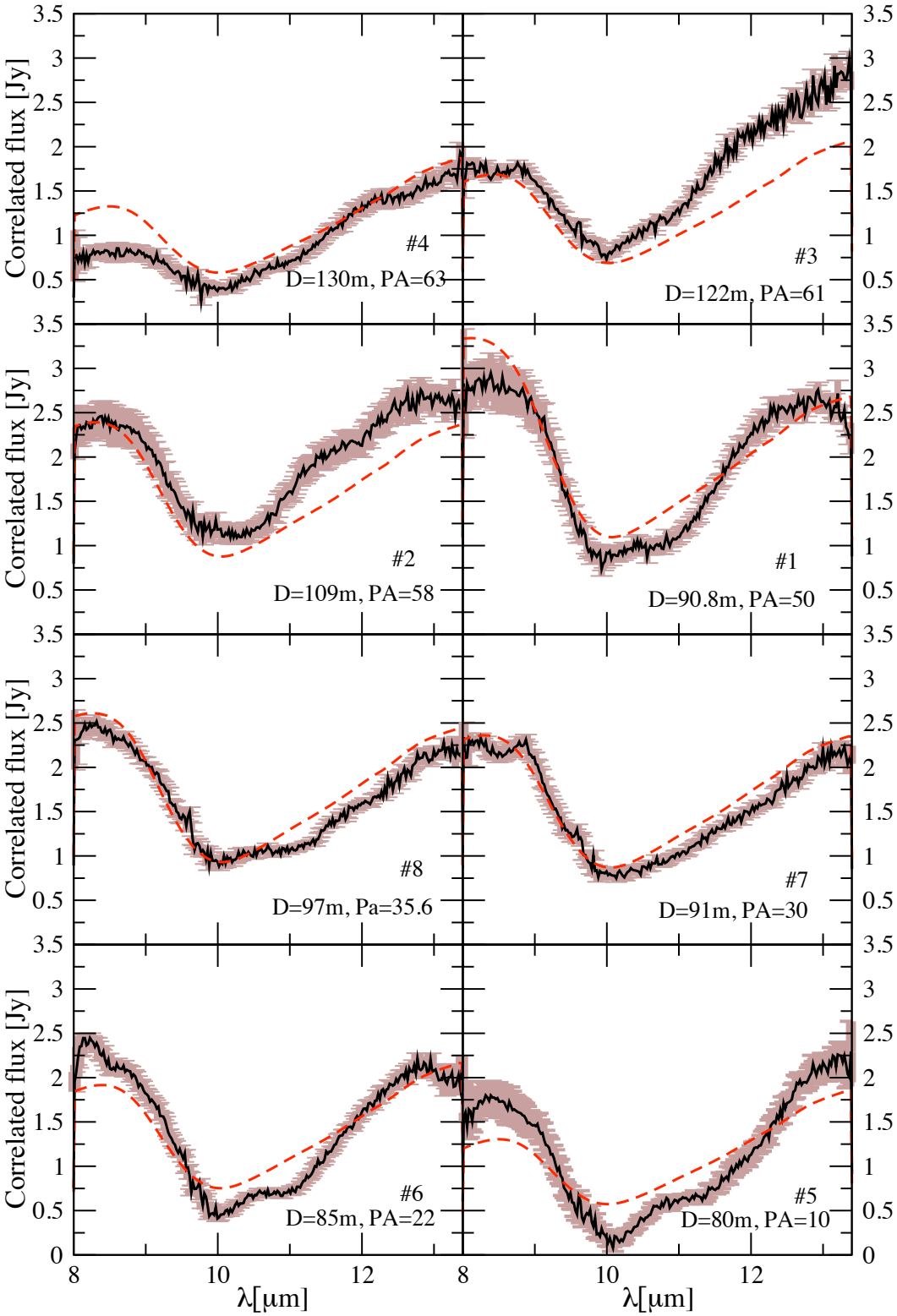

Figure 3.3 — Correlated fluxes #1-8 (solid black) and the model fit from section 3.4.1 (red-dashed). The panels are sorted according to baseline length and the unit telescopes used, and are numbered according to the number in the observation log (Table 3.1).

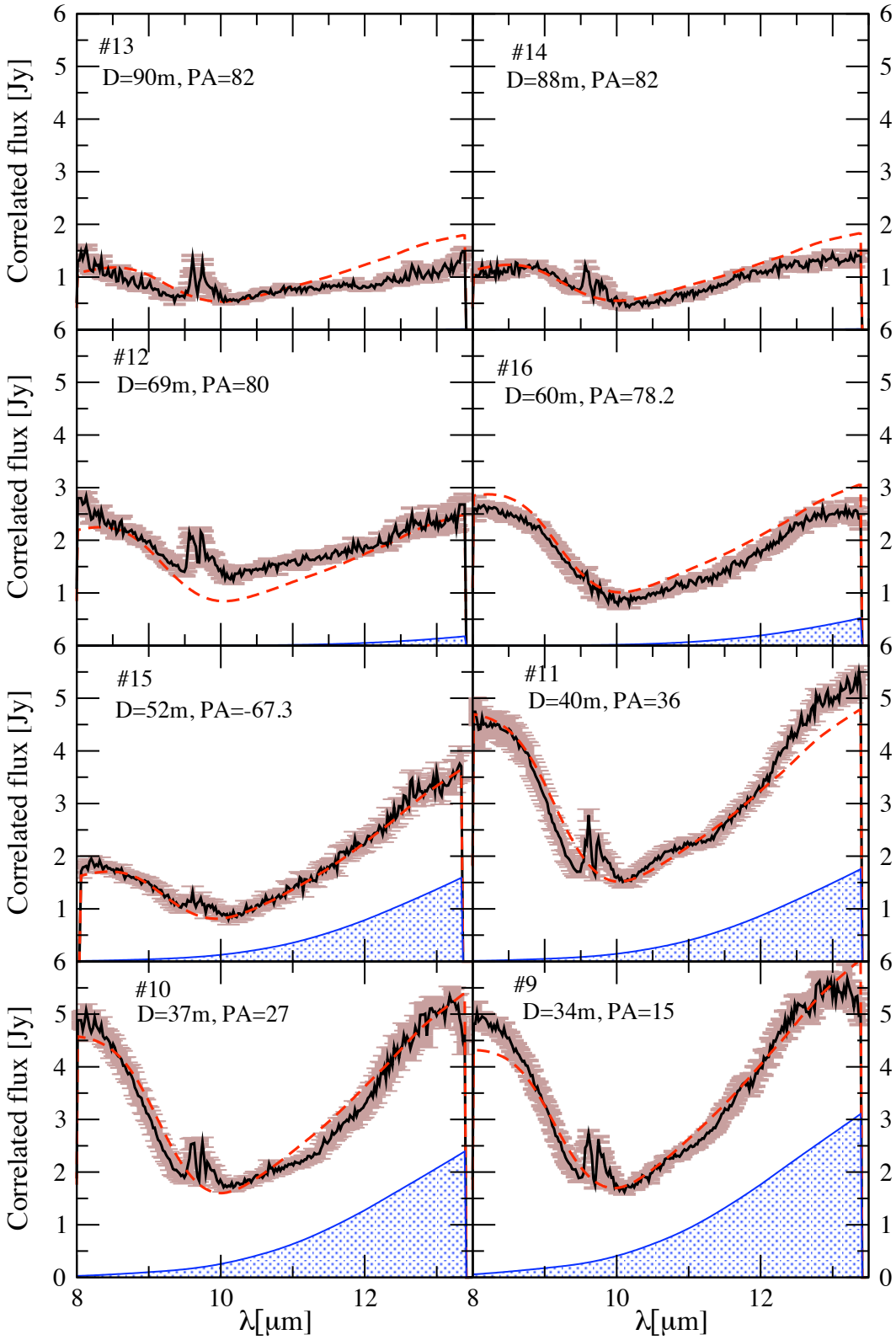

Figure 3.4 — Correlated fluxes #9-16 (solid black) and the model fit described in section 3.4.1 (red-dashed). The blue filled curves show the contribution of component 2 to the correlated fluxes. The 'bump' at 9.7μm visible on fluxes #9-14,16 is due to the atmospheric O_3 feature. The panels are sorted according to baseline length and the unit telescopes used, and are numbered according to the number in the observation log (Table 3.1).

A note on phases and symmetry

Apart from the correlated and total fluxes, one can also recover the differential phase $\phi_{diff}(k)$ of the source from MIDI data. The differential phase is related to the source's true phase, $\phi(k)$, by $\phi_{diff}(k) = \phi(k) - C \times k$, where $k = 2\pi/\lambda$ is the wave number and C is an unknown constant. Thus, any linear dependence of ϕ on k is removed from the differential phase in the data reduction process, and cannot be recovered. This missing information in the differential phase makes it very challenging to include it in our models. We have therefore postponed treatment of the differential phase in NGC 1068 to a second paper. Without the phase information, only models or images which possess inversion symmetry can be applied to the data. Throughout this paper, we assume a symmetric flux distribution. This is an instrumental limitation and we do not claim that the true source brightness possesses such symmetry.

3.4 Modelling

As interferometric data is obtained in Fourier space, interpreting the data is not as straightforward as in direct imaging or spectroscopy. In infrared interferometry, where only a small number of the absolute value of the Fourier components can be measured, the results are often model dependent and difficult to interpret unambiguously. The effective resolution for each uv point is determined by λ/B, the projected separation between the telescopes expressed in number of wavelengths. This relation causes the spectral features of the source, which strongly depend on λ, to become entangled with the spatial flux distribution as observed by telescopes of separation B. We have attempted to disentangle the two effects by using two different modelling approaches. First, we treat the flux distribution as coming from two Gaussian components, each with a fixed size and orientation. Each component is assumed to be a grey body with a fixed temperature and situated behind a uniform absorption screen (§3.4.1). The model results show us that at 8μm only one component contributes to the correlated flux. Therefore, we chose to attempt to reconstruct an image at this wavelength, which is shown and discussed in §3.4.2. The image agrees well with the modelling results. In our third approach (§3.4.3) we look at each wavelength independently and fit a single Gaussian component to each, assuming no relation between the different wavelengths in the data, and assuming all the observed structures in the correlated fluxes arise from the different source sizes and orientation at each wavelength (channel by channel fitting). A good understanding of the observed properties of NGC 1068 can then be achieved by combining the results from the different procedures.

3.4.1 Two grey body model

The first approach to disentangling structure and spectrum is to assume that changes to the correlated fluxes with wavelength are solely due to spectral effects, i.e. a grey body emission undergoing absorption while keeping the spatial parameters constant with wavelength. In this model we treat the infrared emission as coming from two Gaussian grey body components of a fixed size and orientation, each one behind a uniform absorption screen. Two is the minimal number of components necessary to account well for the data, while the addition of more components does not improve

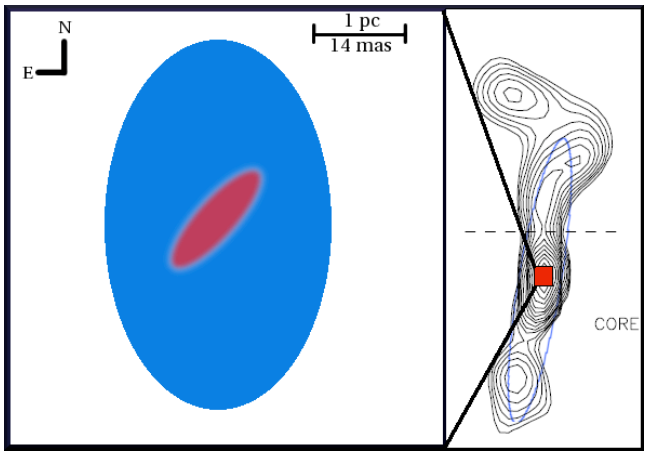

Figure 3.5 — Comparison between the two components in our model and the 12.5μm image of Bock et al. (2000), taken with the 10m Keck telescope. The two components are plotted symmetrically, yet their relative position cannot be determined from the correlated fluxes.

our fit. The correlated flux of each component is given by:

$$F_{corr}(\lambda, u, v) = \eta BB(\lambda) V(u/\lambda, v/\lambda) e^{-\tau \cdot abs} \tag{3.1}$$

where BB($_\lambda$) is the emission from a black body of temperature T; V is the visibility of a Gaussian component whose major axis, minor axis, and PA are to be fitted; abs is the absorption curve of a chosen mineral or a combination of a few minerals as described below. The coefficient η is the grey body scaling factor and has a value $0<\eta<1$, independent of wavelength.

After computing the Fourier amplitudes corresponding to each uv point in the model, the two sets of amplitudes (one for each component) are then combined to produce the final correlated flux to be compared to the data:

$$F_{corr} = |F_{corr1} + e^{2\pi i(ul+vm)} F_{corr2}| \tag{3.2}$$

The parameters l, m are for the two components to be moved with respect to each other in the plane of the sky, parallel to the RA and DEC directions, respectively. In practice we find that the data does not provide constraints for the relative positions l, m (see also §3.4.1.1) and we have set them to zero (concentric components). Each component in the model has six parameters, making in twelve in total: the major and minor FWHM, the position angle ϕ, the BB temperature T, the optical depth τ, and the scaling factor η. The main features of the data can be reconstructed from values of the correlated flux at about six wavelengths, in the sense that if the model fits the data well at those wavelengths it will fit the rest well. We can then estimate that these 12 parameters are in fact fitting $6 \times 16 = 96$ independent data points. The total flux is treated here as an extra uv point to be fitted, and is computed by setting the u and v coordinates in equation 3.2 to zero for each component. In practice we find that the total flux is easily reproduced in many of our models and for a different range of parameters, and may serve as an upper limit to the flux and size of each component. The most difficult part in our model is to determine the absorption curves in equation 3.1. We have selected several dust absorption templates, including standard galactic dust as observed towards the centre of the Milky Way (Kemper et al. 2004), as well as $Ca_2Al_2SiO_7$, which was found to best fit the previous MIDI data (J04, Speck et al.

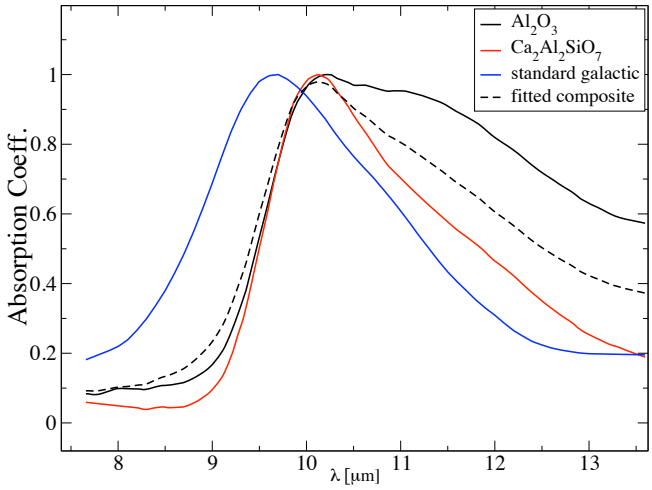

Figure 3.6 — A comparison between the absorption template used in fitting the data (dashed) and the other spectral templates for dust particles commonly found in astrophysical environments. The latter includes that of dust seen toward the centre of the Milky Way. These templates only include line absorption and do not include the continuum absorption.

(2000)). Our aim here is not to unambiguously determine the chemical composition of the dust, which is not possible to do from the data, but rather to characterise the spectral template which will fit the data best, and to compare it with other known dust mineral templates. In this respect the template is any simple function $f(\lambda)$ which, when inserted into equation 3.1, will provide the best fit for the data. To achieve this, we first fit a combination of the minerals listed above and shown in Figure 3.6. The best-fit combination was improved on by allowing the value of τ at several key wavelengths (i.e. 8, 9, 9.7, 11.5 and 13μm) to vary and then interpolated between the new values using cubic spline. This method is able to mimic a typical absorption template. The resulting template, which we designate 'fitted composite', along with several other dust templates are plotted in Fig. 3.6 while the model parameters are given in Table 3.2. The parameter values in Table 3.2 are based on the results of different models that differ in the chemical composition of the dust. To determine the errors we fixed the value of all but one parameter at a time and noted the range of values resulting in significant changes to the model.

We label the two components in our model as components 1 and 2. Figures 3.3 and 3.4 plot the best fit model against the correlated fluxes, while Figure 3.2 plots the model's fit to the total flux plus the contribution from the individual components.

The fitting was done by finding the least-squares solution using the Levenberg-Marquardt technique. The general trend is for the quality of the fit to become worse with increasing baseline length, as one might expect from the lower spatial resolution of a short-baseline observation. In addition, component 2 only contributes to the correlated fluxes taken with shorter baselines, effectively increasing the number of fit parameters. Some of the features in the correlated fluxes, in particular the 'step' seen most clearly in correlated fluxes #4 and 5 at 10.5μm, cannot be reproduced by the simple model we propose. Our model will always generate smooth fluxes due to the smooth absorption templates we use, which not contain any such 'steps'. Furthermore, introducing more complicated templates will not help to fit these unsmooth features since any change made to the templates will affect each correlated flux, while these unsmooth features only appear in some of the correlated fluxes.

Seven out of sixteen modelled correlated fluxes (#7,8,9,10,11,15,16) are in excellent

Table 3.2. Parameter fits for the two grey-body model of §3.4.1.

parameter	value[a]	error	units
Component 1			
FWHM major	20	$\pm$ 3	mas
FWHM minor	6.4	$\pm$1	mas
ϕ	-42	$\pm$ 2	degrees
T	800*	$\pm$ 150	K
τ	1.9	$\pm$ 0.5	
η	0.25*	$\pm$ 0.07	
Component 2			
FWHM major	56.5	$\pm$ 5	mas
FWHM minor	42.4	$\pm$5	mas
ϕ	0	$^{+70}_{-20}$	degrees
T	290	$\pm$ 10	K
τ	0.42	$\pm$ 0.2	
η	0.64	$\pm$ 0.15	

[a]The temperature and scaling factor, η, are not independent. Temperatures as high as 1500K can be fitted with a low scaling factor, η $\sim$0.05, although the resulting fit is not as good.

agreement with the data while the rest of the modelled fluxes are mostly in good to perfect agreement with the data either for λ <10μm or for λ >10μm. The two components are illustrated in Figure 3.5. Given the range of spatial resolutions of the different baselines (spanning a factor $\sim$4 in length), the complex behaviour of the correlated fluxes and the striking simplicity of the model, it provides a surprisingly good fit to the data.

3.4.1.1 Symmetry issues

As stated before, only phaseless and therefore symmetric models were applied to the data. The lack of an absolute phase also implies a loss of astrometric information. We cannot, for example, determine the position of the mid-infrared emission in relation to other known components on similar scales for NGC 1068. In principle, we could constrain the relative position of our two model components by means of the l, m parameters in equation 3.2. If our two components are not symmetric with respect to each other, the resulting phase difference will also affect the sum of the Fourier amplitudes of both components, i.e. the observed correlated fluxes. In practice, we find that we do not have enough information on component 2 in order to determine its relative position. Models with offsets of up to a few tens of mas are virtually indistinguishable from models with zero offsets. In order to better constrain the relative positions, more observations on shorter baselines are needed, as component 2 is mostly over-resolved

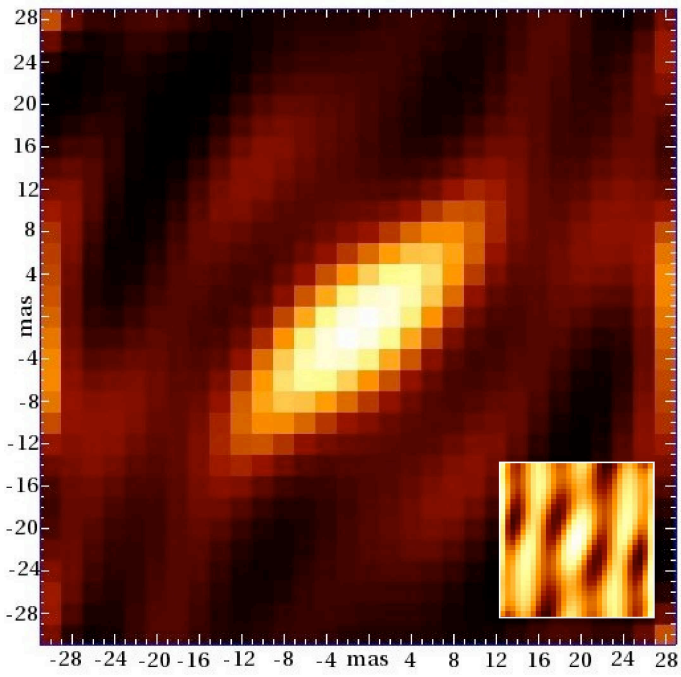

Figure 3.7 — Maximum entropy reconstruction at 8μm. Image size is 30×30 pixels, with 1pix=2 mas. Colour scale is linear. The extended blobs are artifacts caused by the low *uv* coverage. Gaussian fitting to this image measures it to be 7.7 / 21 mas in FWHM with PA=$-46°$, very close values to the grey body model results, and in agreement with the results of the one Gaussian fitting at 8μm. The 'dirty map' is shown in the bottom left corner.

in our baseline sample. We do know from the differential phase that the mid-infrared emission is asymmetrical. However, we cannot tell whether this asymmetry is due to the geometry of the dust clouds or the result of asymmetrical absorption in the torus.

3.4.1.2 The infrared SED

The model used here is specifically designed to explain the MIDI data in the wavelength range of 8-13μm. It is not a full radiative transfer model, and therefore cannot be used to predict or account for the entire infrared SED of NGC 1068.

3.4.2 Maximum entropy imaging

The fits of the two blackbodies presented in §3.4.1 are not perfect fits to the data. Attempting to improve them, we explored different perturbations in the Gaussian distribution and although some of them can make the fit better, they are still ad-hoc. Finally we decided to reconstruct an image using maximum entropy (ME) methods, which guarantees that the resulting image will be the most statistically probable reconstruction given the information in the data. To our knowledge, this is the first time such a method has been used with infrared interferometric data. The ME reconstruction is based on the general algorithm by Skilling & Bryan (1984) and modified to the specific needs of dealing with MIDI data. The code was tested on simulated data with similar S/N as the original data and using the same *uv* coverage of NGC 1068 (Fig. 3.1). In general, the code is able to accurately reproduce Gaussian brightness distributions or similarly simple shapes without sharp edges. Attempting to reconstruct multiple component images (such as a binary) have not been successful for this *uv* coverage. We have chosen to reconstruct the image at 8μm, since in that wavelength a single component fits the data well and the silicate absorption does not come into play. The

resulting image is displayed and discussed in Fig. 3.7. The ME method is useful since it is not model-dependent and no prior assumptions about the source are needed to make use of it. Although the ME image details the basic properties of the source, and can provide a good starting point for any model, it does not provide a more detailed picture than parametric models which enable us to probe the wavelength dependence of the data as well as its brightness distribution. Nevertheless, the ME image does fit the data set at 8μm perfectly. Since the code, by definition, always prefers to get rid of complicated structures, we can gain insights into the deviations from the pure Gaussian shape in our models by looking at how the code chooses to reduce the χ^2 of the image. The central shape in the image fits well with component 1 from §3.4.1, while the extended blobs seen are needed to perfect the χ^2. We believe that the blobs correspond to extended emissions present in the source, while keeping in mind that the specific shape and positions of the blobs mostly reflect the low *uv* coverage of the data set. The contribution of the extended emission, as measured from the intensities in the image, is about 15% of the flux of component 1.

3.4.3 Channel by channel Gaussian fits

MIDI uses a grism to disperse the two beams into 261 channels before combining them. Per channel per time, we have a set of 16 correlated fluxes, or Fourier amplitudes, one for each baseline. From these amplitudes a Gaussian brightness distribution corresponding to infrared emission from this channel's wavelength is fitted. The fitting is done directly in the *uv* plane, and takes into account only the correlated fluxes. In each wavelength we fitted a single Gaussian, motivated by the successful Gaussian fitting of J04 to data composed of two baselines. The fit results are summarized in Fig. 3.8, which plots the values of the model's parameters (i.e. the major and minor FWHM sizes, height and position angle of the fitted Gaussian) and the resulting normalised χ^2 for each fit, determined by dividing the χ^2 by the number of degrees of freedom (16) minus the number of model parameters (4). The main results from this approach are:

1. The FWHM major and minor axis (Fig. 3.8a) lengths increase with wavelength. This is expected of centrally heated dust since longer wavelengths indicate cooler temperatures. and therefore larger radii. For optically thin dust in radiation equilibrium where $T \propto r^{-0.5}$, and for blackbody emission where λ scales as $1/T$ (Wien's law), we get $r \propto \sqrt{\lambda}$ as a crude estimate, which fits the trend seen in the fitting of the Gaussian's axis. The discontinuity at $\lambda \simeq 9.5\mu$m is due to the atmospheric 9.7μm Ozone feature and the intrinsic Silicate absorption.
2. The Gaussian flux density (Fig. 3.8b) is simply a response to the varying flux with wavelength.
3. The Gaussian's position angle (Fig. 3.8c) is perhaps the most interesting of results. First, we fit the same position angle from 8 to 9μm, followed by a jump of $\sim$10 degrees, which gradually rotates back but does not return to its original angle. The location of the jump in the position angle is indicative of the wavelength at which the Silicate absorption feature takes effect. The gradual, linear change in the position can be most easily interpreted as asymmetrical absorption, i.e. the absorption at 9 micron is more pronounced to the south-west of the Gaussian than at 12μm. In contrast, a constant PA will indicate a uniform absorption screen

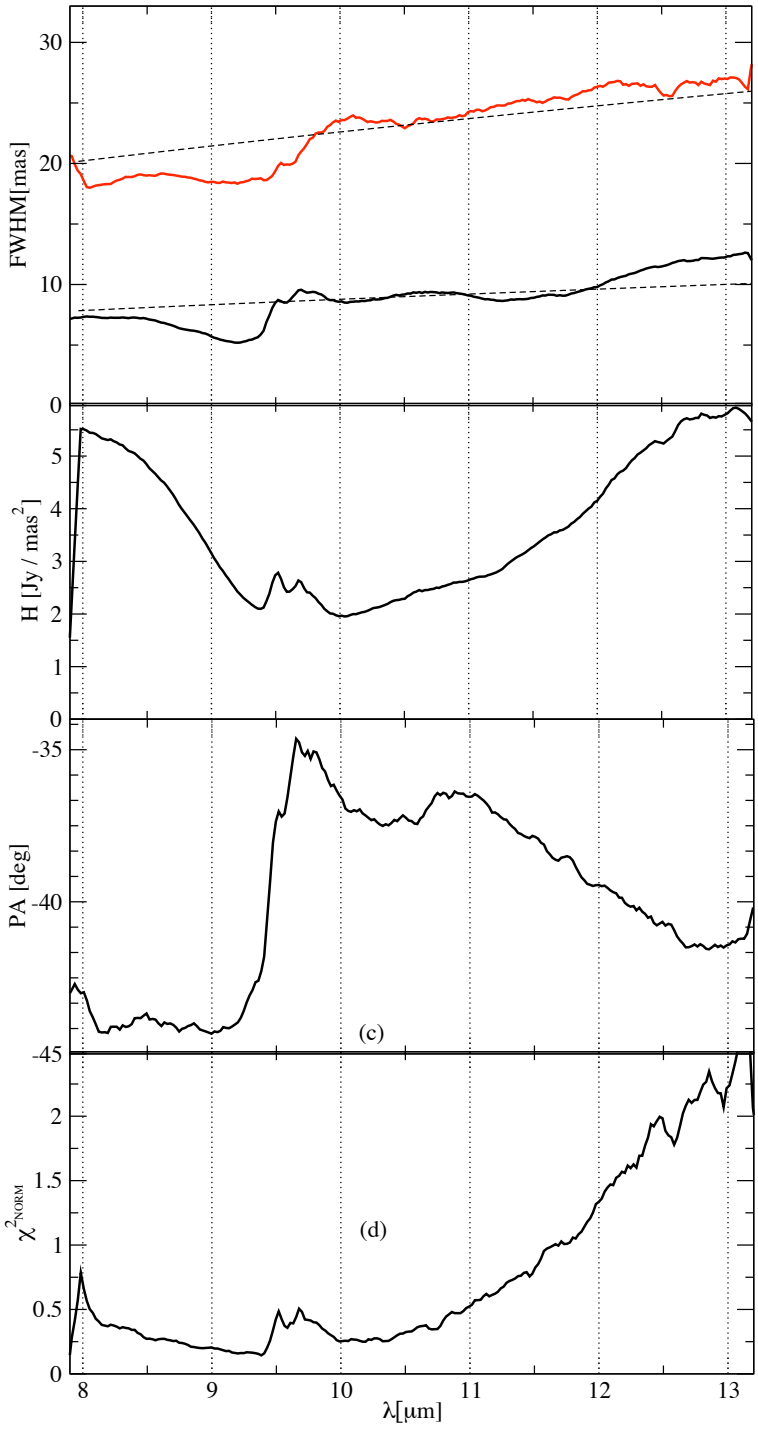

Figure 3.8 — Results of one Gaussian fitting. (a) FWHM sizes for the major (red) and minor (black) axes, overlaid with $r \propto \sqrt{\lambda}$ (dashed); (b) Gaussian peak; (c) position angle and (d) normalised χ^2, for each wavelength. We stress that in this model each wavelength was fitted independently, and the χ^2 in panel (d) is the minimized χ^2 found for each wavelength. The 'bumps' near 9.7μm are caused by the O_3 atmospheric feature.

is effectively present.

4. Further, we can deduce the presence of another dust component from the difference in PA between 8 and 13μm. The χ^2 (Fig. 3.8d) also supports the presence of an additional component, gradually becoming worse from 10μm (with increasing wavelengths). Although we cannot determine the geometry of this second component from this method, we can estimate that it consists of warm ($\sim$300K) dust, whose blackbody emission begins contributing to the flux at $\lambda >$10μm.

In general, the single Gaussian per wavelength model fits the data well, and helps to reduce the complex behaviour of the correlated fluxes to a set of four parameters that vary with λ. It is, however, a geometrical model and does not relate the different wavelengths in a physical way. We find it encouraging that the different parameters are continuous and behave in an 'orderly' fashion, although fitted independently.

3.4.4 The properties of each component

We now discuss in detail the properties of each component in the model, combining results from the different modelling methods.

3.4.4.1 Component 1

Component 1 is the dominant source of Mid-infrared emission on MIDI's scales. It is resolved in all of our observations and its geometrical properties are well constrained to have a major axis of 20 and a minor axis of 6.4 mas in FWHM with a PA=-42°. As Table 3.2 shows, and in contrast to the second component, the temperature and optical depth are not well constrained. Nevertheless we can establish that component 1 is composed of hot dust (T$\simeq$800K), with a low scaling factor ($\eta \sim$0.2). Although we cannot unambiguously determine the chemical composition of the dust, we observe that it differs from the profile of standard interstellar dust. Namely, the dust should begin absorbing towards 9μm and the optical depth should rise more sharply towards 10μm, followed by a shallower decline up to 14μm. Figure 3.8c indicates asymmetric absorption toward lower position angles, which may explain the deviations from a 'perfect' fit in both our models for the wavelength range $\lambda >$10μm. **Clumpiness:** Evidence for clumpiness comes from the small scaling factor, which is consistent with clumpy emission on unresolved scales that effectively reduces the surface brightness of the source independently of wavelength. Attempts to fit the data with models where the scaling factor is close to unity have not been successful. Extinction in the mid-infrared towards our line of sight probably contributes to the low value of η, but cannot fully account for it without invoking clumpiness. More direct evidence for clumpiness comes from the profile of the correlated flux of *uv* #4 at 8 μm, which is significantly less than our Gaussian model predicts. This is the observation with the longest baseline and as such it is most sensitive to small scale structure such as clumps. Given a resolution of 5.8 mas at 8μm for that baseline, we set an upper limit of 0.4pc (5.8 mas) for the size of a clump. Alternatively, one can interpret the missing flux at that *uv* point as a smooth (rather than clumpy), non-Gaussian flux distribution at sub-parsec scales.

3.4.4.2 Component 2

Since most of our observations were taken with long baselines, component 2 is mostly over-resolved. Figure 3.4 (filled curves) plots the contribution of this component to the correlated fluxes, illustrating its presence in only five of the sixteen baselines observed, corresponding to those shorter than sixty meters in telescope separation. As a result, its geometrical properties are not well constrained, while the temperature prediction is confirmed by that found in §3.4.3. As for the size of the flux distribution, component 2 is an extended Gaussian structure, with a minor axis of 42 mas and major axis of 56 mas in FWHM. It's orientation is best fitted as north-south, with a large uncertainty. Component 2 marks the colder, extended part of the torus-like structure, and is (together with comp 1) the unresolved source reported by Poncelet et al. (2007) and others (see introduction). Its north-south elongation is common with elongation of the mid-infrared tongue (Figure 3.5) of NGC 1068, which Bock et al. (2000) attribute to re-emission by dust and UV radiation concentrated in the ionization cone.

3.4.4.3 The physical distinction between the components

In our model the two components are separate and distinct, each with a fixed temperature. In reality, we expect the dust, on average, to have a smooth temperature and density distribution contained in one structure. In this sense, the two components are an abstraction. However, our findings here, and in particular the quality of the fit to the data, indicate that the two-component approximation is accurate regarding the brightness distribution of the dust, and this requires a steeper temperature gradient than the simple $T \propto \lambda^{-0.5}$ expected for centrally heated, optically thin dust.

3.4.5 Summary of modelling results

To summarise our main findings, the mid-infrared emission from the core of NGC 1068 within a beam size of 28 mas (∼2 pc) is dominated by a warm Gaussian-shaped structure of dust (comp 1) with a chemical composition unlike that of dust towards our own galactic centre. The geometrical properties of this component are independently well constrained in each of our methods of investigation. Component 1 is co-linear with, and has similar size to the H_2O megamaser disk. It is tilted by $\sim 45^\circ$ to the radio jet, and perhaps also by a lesser amount (∼15°) to the ionization cone. The dust temperature is ∼800K, assuming a grey body model. Evidence for clumpiness is mostly indirect, and comes from the low grey body scaling factor and the deviation from a Gaussian fit for data obtained with the longest baseline. This single Gaussian component cannot account for the total flux as observed with an 8m telescope, as shown in Figure 3.2. It also does not fit the data as well for wavelengths longer that 10μm on our shortest baselines, suggesting the need for a second component (comp 2), which is extended so that it will become over-resolved with baselines longer than 60m. The filled curves in Figure 3.4, which plots the contribution of component 2 to the correlated fluxes, demonstrates how small that contribution is. As a result, the geometrical properties of this component, including its Gaussian nature, are not well constrained.

3.4.6 Comparison with previous MIDI studies of NGC 1068

Two previous studies of the core of NGC 1068 have been made using MIDI. Both studies were based on the same set of data: two *uv*-points with baseline lengths of 42 and 72 meters, obtained during the science demonstration time of the instrument. They were taken with the PRISM mode, which offers a low spectral resolution of $\lambda/\delta\lambda \simeq 30$. The first study, by Jaffe et al. (J04), used a simpler version of the two Gaussian grey-body components used in this work (§3.4.1), and their findings are summarised in the introduction. In general, our findings here agree with those of J04, deviating from their results only in one parameter: the orientation of the extended component (component 2), which was then reported to be elongated east-west. This discrepancy is not surprising in light of our finding here that the extended component is over-resolved in observations with baseline lengths longer than 60m. This leaves just one observation (in J04) where component 2 contributes significantly to the correlated flux, not enough to determine its orientation. The FWHM sizes of the extended component in Jaffe et al. (30 and 49 mas) are smaller than the sizes reported here, and so the component was able to contribute to the correlated flux obtained with the longer baseline (72m), and an estimation of its orientation and axis ratio could be made. The second study, by Poncelet et al. (2006) (hereafter P06), used a different approach to modelling the same data set. Instead of Gaussian components, P06 used a combination of two uniform, circular disk components and visibilities rather than correlated fluxes as the quantity to be fitted. The derived angular sizes and temperatures of the two disk components are $\sim$35 and 83 mas, and $\sim$361K and 226K, respectively. Both approaches provided good fits to the data from the two short baselines. This is because the differences between a Gaussian model and a uniform disk is small for short baselines. With the addition of data taken at longer baselines, we can now determine that the circular disk model of P06 is inconsistent with the MIDI data presented here. This is mostly due to the sharp edge of the circular disk model: the visibility (and the correlated flux) of a circular disk is proportional to the absolute value of the J-Bessel function of the first order, which goes down to zero at specific baselines depending on the angular size of the disk and the baselines length in units of the observed wavelength. For the disk sizes of the P06 model, these zeroes fall between baseline lengths of 60m (at 8μm) to 100m (at 12.8μm), a range which is well sampled by our observations. Yet, no trace of the drop in the correlated flux predicted by the uniform disk model is seen in any of our observations. The zeroes in the visibility function appear for any flux distribution that possesses a sharp edge. Thus, our data is inconsistent with any such flux distribution.

3.5 Discussion

NGC 1068 is considered as the prototypical Seyfert II galaxy. It is also the first Seyfert II with broad emission lines seen in polarized, scattered light (Antonucci & Miller 1985). These observations proved that NGC 1068 harbours an obscured Seyfert I nucleus, and led to the AGN unification model, at least in its most simple form, uniting Seyfert I & II nuclei. This is **the** object for which the obscuring dusty torus was originally invented. The previous sections have described the *appearance* of this structure at mid-infrared wavelengths and sub-parsec scales, and its geometric relation to structures

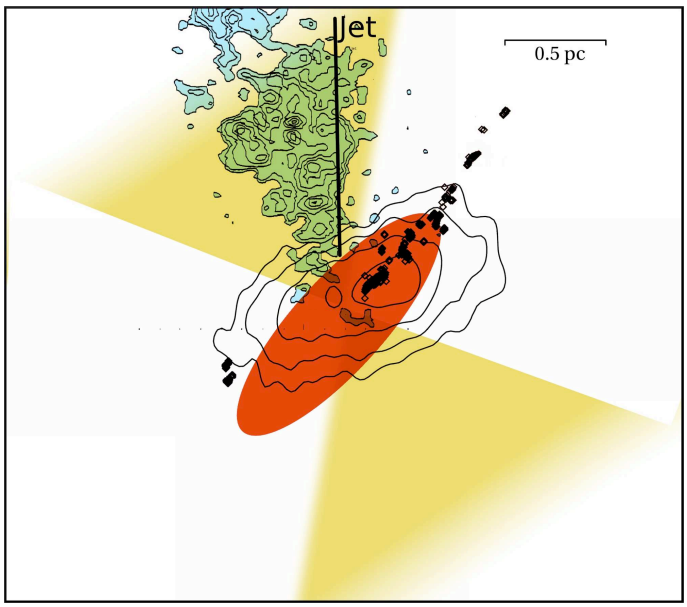

Figure 3.9 — Picture summarising the multi-wavelength structures on parsec-scales in the nucleus of NGC 1068. The FWHM of the compact dust (component 1) is sketched in red, centred around the H_2O maser spots and 5GHz radio emission, both from Gallimore et al. (2004). Contour levels below the FWHM level have been removed to allow a better comparison between the radio and the mid-infrared. The ionization cones inferred from spectroscopy by Das et al. (2006) are shown in yellow, and the HST [OIII] (**reduced in scale by a factor** ~ 100) image contours (Evans et al. 1991) are shown in blue to indicate the visual orientation of the cone.

seen at other wavelengths.

The literature on the spectrum of NGC 1068, both observational and theoretical, is very extensive. Many authors have modelled the production of the overall SED of the galaxy within the context of the unified theories. Without detailed structural observations, however, they have found the problem underconstrained. The early interferometric work of J04 and W04 led modellers of the emitted spectrum in the direction of collections of optically thick inhomogeneous ("clumpy") systems. Following the pioneering work of Nenkova et al. (2002) on clumpy models, Hönig et al. (2006) and Schartmann et al. (2008) showed that three-dimensional radiative transfer models of clumpy tori were consistent with the low spatial resolution SED data and the J04 interferometric data of NGC 1068. The Hönig et al. (2006) model of a torus with an inclination of $i = 55°$ is also able to fit the K-band measurements of W04 to a factor of 2 in correlated flux. In a later work (Hönig et al. (2007)) the authors have revised the inclination angle of the torus to $i = 70°$, this time providing excellent fits to both the SED and the previous interferometric N-band data, though still falling short of reproducing the K-band interferometric data. Most recently, a model with an edge-on torus ($i = 90°$) was presented (Hönig et al. (2008)). This model was fitted to the SED and one of the interferometric data points of J04, reproducing a good fit to the former, and a fit correct to a factor of $\sim$2 for the latter. Their most important conclusion is that the random cloud arrangement has a significant effect on the SED and images, providing remarkably different SEDs for different cloud arrangements and for the same set of large-scale torus parameters. This accounts for the difficulty in determining the inclination angle.

The observational material presented here is considerably more detailed than that which was available to the authors cited above, and the results of their simulations of the production and redistribution of the radiative energy are generally not presented in a form that can be directly compared to our measured correlated fluxes as a function of wavelength and baseline and position angle. Hence, while these models seem globally consistent with our present data, we refrain from considering whether any of them do

or do not *fit* it in detail. Rather we focus on the physical structures we observe and their relations to the surrounding AGN components. We also consider the similarities and differences of the results for NGC 1068 with those of the nearby Circinus Seyfert II galaxy, (Tristram et al. 2007), and compare the implications of our N-band data with those measured on the same galaxy by W04 in the K-band.

3.5.1 The inclination and thickness of the dust

In this section we argue that the nuclear dust structure in NGC 1068 is circum-nuclear and inclined edge-on, and therefore its observed size and the 3:1 ratio of its major/minor axis is indicative of the thickness of its inner part rather than a projection effect of an inclined disk. Our main argument here is that the dust and the maser disk are co-spatial, and since the masers are seen edge-on, so is the dust. The possibility of detecting the hot dust through the cold dust that surrounds it has been demonstrated by several recent three dimensional radiative transfer calculation of tori:
Schartmann et al. (2005) find that "in a homogeneous dust distribution the observed mid-infrared emission is dominated by the inner funnel of the torus, even when observing along the equatorial plane". Similar results are also found by Hönig et al. (2006) and discussed in more detail in section 3.4.6. We show that this scenario of an edge-on geometrically thick torus not only agrees with 3D radiative transfer models, but also is consistent with other observed structures on milliarcseconds scales:
(a) The position angle of component 1 is virtually the same as the PA of the western maser spots. This can hardly be a coincidence. The theoretical relationship between water maser excitation and warm molecular dust has been well established (Neufeld et al. 1994, for example), and the masers are indeed expected to be embedded in warm ($>$600K) molecular dust.
(b) Apart from the position angle, the inner radius of the maser disk is approximately the radius at which dust sublimes (Greenhill 1998). Dust reverberation modelling for the maser disk (Gallimore et al 2001, Fig. 9) has established the geometry of the masers, with those closest to the nucleus outlining a ring 0.6 pc in radius. The diameter of the ring (1.2 pc) is similar to the FWHM size of the major axis of our component 1 (1.35 pc), supporting the conclusion that the masers and the hot dust component are co-spatial.

3.5.2 The orientation with respect to the jet

Although there seems to be little or no correlation between the relative angle of jets and the dust residing in the galactic disk for Seyfert galaxies (Kinney et al. 2000), the naive expectation is that the dust directly orbiting the black hole and the accretion disk is perpendicular to the jet. It is the common belief that the orientation of the jet is closely coupled to the spin axis of the black hole, which in turn is affected by the sum of all the angular momenta of the material accreted throughout its lifetime. Capetti et al. (1999) estimate the lifetime of the jet as $<1.5\times10^5$ years, a much shorter time compared to the lifetime of the black hole. The current phase of the AGN is not likely to have affected the spin axis of the black hole, and it is not surprising that the dust and the maser disk are not aligned with the jet. Still, it is interesting to consider the origin of the orienta-

tion of the dust component and the maser disk, since it seems related neither to the jet nor to the galactic plane. We now consider two mechanisms:
self warping. The sub-Keplerian velocities of the masers have been interpreted as evidence that the disk is supermassive and will warp due to self-irradiation (Lodato & Bertin 2003). This mechanism, however, only applies to thin structures and therefore cannot account for the orientation of the dust.
misaligned inflow. In this scenario the matter falls misaligned with respect to the current orientation of the jet. This can be the result of either matter infalling from outside the plane of the galaxy, or due to the influence of a torque, perhaps from a non-spherical nuclear star cluster. The presence of such a potential will be most likely due to a past minor merger, for which some evidence exists (Garcia-Lorenzo et al. 1997). Observations so far have determined that a dynamical mass of $6.5 \times 10^8 M_\odot$ is present inside a 50 pc radius (Thatte et al. 1997), but due to obscuration by dust there is no information on the gravitational potential at smaller scales. This mass is about 12 times the mass of the black hole (Lodato & Bertin 2003), and at a distance a few parsecs the black hole's potential still dominates over the potential of the star cluster. The influence of a star cluster may also explain the non-Keplarian velocity distribution of the masers. Finally, the generally linear, stable shape of the jet excludes non-continuous capture of material into the black hole such as individual stars or individual dust clouds, which may take an arbitrary route. To conclude, the identical orientation of both the thin maser disk and the thick dusty torus strongly indicate that it is the angular momentum of the infalling matter combined with the gravitational potential at the nucleus that are responsible for the current orientation of the maser (i.e. accretion) disk and the inner part of the dusty torus that surrounds it. When discussing the orientation of the central dust component and the orientations of other components related to the nucleus, it is interesting to point out that Galliano et al. (2003) have proposed to explain the asymmetrical appearance of the H_2 brightness distribution (on arcsecond scales) by suggesting that the Compton thick material located in the very central parts of the AGN is tilted with respect to the large scale molecular gas distribution with an orientation of 30 degrees, which is comparable to our findings.

3.5.3 Relation between the torus and the ionization cone

According to the AGN unification scheme, it is the obscuring torus that is responsible for the conical shape of the ionized gas in the narrow line region since it blocks the UV radiation from ionizing the material outside the cone. The cone's opening angle and orientation are then related to the orientation and geometry of the torus, and in particular to the arrangement of the clouds in its inner edge. Now that the inner part of the torus has been resolved, we can compare the two quantities and relate them to the predictions of the unification model. The position angle of the dust is well constrained to be -42° (see Table 3.2). We then expect the ionization cone to be centred perpendicularly (i.e. at PA=48°). The opening angle in this scenario depends mainly on the inner geometry of the torus, as each cloud in itself is optically thick to UV and X-rays, and trivial geometrical considerations limit the cone's angular extent to within $\pm 90^\circ$ of the torus axis (i.e. -42<PA<138).

The ionization cone, as seen in HST (Hubble Space Telescope) images, is centred

around PA=10°, with a small opening angle of $\sim 45°$ (see Evans et al. 1991, for example). As we can see in Figure 3.9, its axis of symmetry is not aligned with the axis of component 1, as it lies about 40 degrees further to the north. Yet, due to its small opening angle, the cone's angular extent is still within the bounds listed above. This discrepancy may be resolved by looking at the kinematics of the outflowing gas. Das et al. (2006) have applied bi-conical outflow models to high-resolution long-slit spectra of the narrow-line region obtained with the Space Telescope Imaging Spectrograph aboard the HST. These models require the cone to have a wider opening angle, $\sim 80°$, centred around PA=30°, rejecting models with PA=10° (Das, *private comm.*), and in agreement with the orientation of our component 1. Figure 3.9 plots the HST image on top of the kinematic model. The northern edge of the cone coincides in both the model and the image, and it appears as if only half of the bi-conical outflow described by the model is seen in the HST image. The UV radiation which ionizes the gas in the cone is partially blocked by the obscuring dust closest to the AGN and is therefore sensitive to the configuration of the obscuring clouds. It is not unreasonable to suggest that some of the UV radiation is blocked by a cloud of dust so that only a part of the gas in the cone is ionize, as seen in the HST images. Assuming this, the orientation of the dust component and the ionization cone roughly match our expectations and give further support to our interpretation of component 1 being the inner hot funnel of the torus-like obscuring object. This implies irregularities in the dust distribution and supports the idea of a clumpy dust distribution.

If this scenario holds then we expect a difference between the appearance of the cone in the optical and in the infrared. The infrared cone (i.e. narrow line region - NLR) should appear more symmetrical with respect to the dust since its appearance does not depend on the ionization of its material. The 12.8m image of Galliano et al. (2005) shows extended emission that is quite symmetrical to the north and the south of the central engine, although the northern emission is considerably more pronounced. The emission is centred on PA=$\sim$27 degrees, which is more symmetrical with respect to the dust, with a relatively small opening angle of $\sim$50 degrees. Alternatively, Poncelet, Sol & Perrin (2008) study the gas dynamic inside the NLR by looking at several mid-infrared emission lines by extracting spectra along two slit positions. They find the infrared cone to be centred on $PA = 10°$ with an opening angle of $\sim$80°. It seems then that in the infrared there is also disagreement between different methods of investigation. A case against this scenario of partial obscuration comes from the well defined shape of the cone over a scale of a few hundred pc, along with the linear shape of the radio jet both suggest that these irregularities in the dust distribution are stable over $\sim$1500 years.

To conclude, observations at infrared vs. optical wavelengths, and emission line analysis vs. imaging all disagree on the properties of the ionization cone / NLR. Further investigation is needed in order to clarify this puzzling aspect.

3.5.4 The dust and the radio emission

Radio observations at 5 and 8.4GHz of the nucleus of NGC 1068 show a parsec-sized component (hereafter: 'radio component'), most likely indicating free-free emission from the X-ray irradiated accretion disk (Gallimore et al. 2004). If so, we expect the ra-

dio component to have similar geometrical characteristics to our component 1. Figure 3.9 shows the 5GHZ contours (up to the FWHM level) against the FWHM of component 1. The radio component is 'thicker' with a major:minor ratio of $\sim 2:1$, as opposed to $3:1$ for component 1 with its PA of -57 degrees. The two components are indeed similar in size and orientation.

3.5.5 Comparison with Circinus

It is interesting to compare our findings with those for the nucleus of the Circinus galaxy, the only other active galactic nucleus for which the central mid-infrared source was studied in similar detail. The Circinus galaxy is similarly regarded as one of the typical representatives of a Seyfert II galaxy population. It shows many of the characteristic attributes of Seyfert II sources, such as narrow and broad emission lines (Oliva et al. 1994, 1998), an ionization cone (Veilleux & Bland-Hawthorn 1997), as well as a 0.4 pc edge-on, warped disk of H_2O masers (Greenhill et al. 2003). At about 4 Mpc, the Circinus galaxy is located significantly closer to us than NGC 1068. However, due to its lower nuclear luminosity, $L_{\rm acc} = 10^{10}\,{\rm L}_{\odot}$ (Tristram et al. 2007), it appears slightly fainter in the mid-infrared than NGC 1068. Using an approach to analyse the MIDI data similar to the one used by us for NGC 1068, Tristram et al. (2007) have found the dust in the nucleus of the Circinus galaxy to be distributed in two components: (1) a dense, warm (∼330K) component of 0.4 pc size and (2) a slightly cooler (∼300K), geometrically thick torus component with a size of 2.0 pc. The model fits to the data were improved by introducing clumpy-like perturbations in the flux distribution, mainly of the larger component, thereby providing arguably the first direct evidence of a clumpy structure in an AGN torus.

As for NGC 1068, the compact component coincides with the nuclear water maser disk in orientation and size and there is evidence for a clumpy or filamentary distribution of the dust. Hence there seems to be some similarity between the dust distributions in these two Seyfert galaxies. Especially striking is the agreement between the sizes when considering that the torus size is expected to scale with the square root of the luminosity of the central energy source, and the identical orientations of the dust and the masers. However, when the properties of the dust distributions are compared in more detail, there are several aspects in which the dust distribution in NGC 1068 deviates from that of the Circinus nucleus significantly. In the first place, while the temperatures of the extended components in the two galaxies are comparable, the compact component in the Circinus galaxy is significantly cooler ($T = 330$ K) than the one in NGC 1068 ($T = 800$ K). The shallow temperature decrease of the dust in the Circinus galaxy was attributed to a high degree of clumpiness in the torus (Schartmann et al. 2008). In fact, this torus seems to be lacking a significant amount of truly hot dust. And indeed, we are observing different physical dust structures: in NGC 1068 the compact component is interpreted as the dust in the inner funnel of the torus, which is heated up to near sublimation temperature. In the Circinus galaxy, on the other hand, the compact component is interpreted as a disk-like dust structure in the centre (or 'midplane') of the otherwise geometrically thick torus. This structure is co-spatial with the rotating disk of maser emitters. As a second difference, in the Circinus nucleus, there is less silicate absorption in the compact component than in the extended component.

This was interpreted to be due to the silicate feature in emission, as is expected from optically thin dust in the inner regions of the torus. In NGC 1068 the inverse is the case, the absorption feature deepens for the compact component. This, and the unusual spectral characteristics of the dust in NGC 1068, as opposed to the dust in the Circinus galaxy that was found to fit that of standard galactic dust, suggest the reprocessing of dust in NGC 1068, in analogy to the evolution of dust in protoplanetary disks. Several underlying properties can have a major influence on the observed temperatures and absorption depths: among them are the total luminosity of the central energy source, the exact inclination angle of the torus, and the volume filling factor of the torus. Proper radiative transfer calculations for the dust distributions in these two Seyfert galaxies are needed to bring more light to this issue. The relationship between the inner dust component and the maser disk found in both galaxies is the most striking of the features both objects have in common, and it may be that this is indeed the generic case in all Seyfert nuclei that also possess maser disks. To conclude, the existence of a thick configuration of obscuring dust was confirmed in both Circinus and NGC 1068. Both dust configuration are found to fit a two component Gaussian model with differences mostly in the temperature of the components, and both components are similarly related to the water maser disk and the ionization cone.

3.5.6 Comparison with other infrared interferometric measurements

This galaxy has been observed previously in the infrared with interferometric resolution in the N-band by us (Jaffe et al. (2004)) and in the K-band by Wittkowski et al. with the VINCI instrument, (Wittkowski et al. (2004) W04), and in speckle mode by Weigelt et al. (2004). These last observations were restricted to effective baselines shorter than 6 meters by the telescope used, corresponding to ~ 24 meters at our shortest baseline at 8 μm wavelength. Thus they are primarily sensitive to structures larger than any observed here, and we will not discuss them further. Here we summarize the findings of W04 and discuss possible nuclear structures that are consistent with both their observations and those reported here.

W04 found a squared visibility of 0.16 ± 0.04 at a projected baseline length of 45.8 meters and position angle of 44.5 degrees, corresponding to a resolution of $\sim$5 mas. The authors favour a multi-component model where 52 mJy originates in an unresolved source of size $\lesssim$5 mas and 75 mJy arises on scales of the order of 40 mas or larger. Again this larger component will not be discussed here. The smaller emission was attributed to thermal emission from hot (1000-1500 K) dust at the inner cavity of the torus, with a possible contribution of direct plus scattered light from the central engine. The resolution achieved by VINCI at 2.2 μm is only $\sim 30\%$ smaller than that we reach on our longest baseline, 129 meters at our shortest wavelength, 8 μm, thus in spatial terms the measurements can be compared directly.

The interpretation of these measurements is clouded by several uncertainties. First, the interferometric observations provide no direct positional information. Thus we do not know the position of the small K-band component relative to the galactic nucleus or relative to the extended features seen with MIDI, except that it must lie within the 56 mas field of view of the VINCI fibers, presumably centered on the nucleus. Second, the extinction in front of the K-band component is uncertain. If this component is seen

through the same extinction as our Component 1 (Table 2), then the K-band absorption may be estimated by scaling the depth of the silicate absorption by a standard extinction curve (c.f. Schartmann et al. (2005), Fig. 3), yielding an optical depth of $\tau_K \sim 3$ but with large uncertainties, particularly if the dust is of non-standard composition. If the K-band component is not at the nucleus, e.g. represents a clump of warm dust clouds as suggested by W04 and Hönig et al. (2008), then perhaps our line of sight to it does not pass through the main body of dust absorption, and the extinction could be significantly smaller. Third, as we have seen in Section 4, the short wavelength, long baseline MIDI results can be well modelled by a smooth gaussian of size 20$\times$ 6 mas, with no evidence of unresolved emission corresponding to that found by VINCI. However, the low scaling factor of Component 1, $\alpha = 0.25$ (Table 2), points to the possible existence of substructure on size scales below the resolution of MIDI. For the 8 μm flux of any of the sub-components we can then only set an upper limit of ~ 750 mJy corresponding to the correlated flux seen on a 129 meter baseline (Figure 3, panel 1). Assuming again a standard extinction law, its intrinsic 8 μm flux would be $\lesssim 1.3$ Jy.

Under these circumstances, we consider only two possibilities for the K-band source where reasonable additional assumptions can be made concerning the above uncertainties: either emission from the accretion disk around the central black hole, or from a small body of hot dust, as discussed by W04 and also proposed by Hönig et al. (2008).

3.5.6.1 Central Accretion Disk

In this case we assume that the source lies behind the absorption seen in N-band and assume that for the intrinsic flux from the accretion disk $S_\nu(2.2\mu) = 0.05 \times e^3 = 1$ Jy and $S_\nu(8\mu) \leq 1.3$ Jy. This would correspond to a $\nu^{-0.2}$ spectrum, not unreasonable for an accretion disk. In addition, this accretion disk flux is consistent with the total accretion disk luminosity: From the total infrared emission $\int \nu S_\nu d\ln\nu \simeq 2.5\ 10^{15}$ Jy Hz (estimated from the data assembled in the *NASA/IPAC ExtraGalactic Database*) one infers the bolometric emission of the disk to be $\nu S_\nu(peak) \sim 7 \times 10^{15}$ Jy Hz (assuming that the UV luminosity exceeds the IR luminosity by a factor ~ 3, because light emitted out of the torus plane is not reprocessed into the infrared). At a distance of 14 Mpc this corresponds to $\sim 1.5\ 10^{45}$ erg s^{-1}, similar to other estimates of the bolometric luminosity of NGC 1068. Schartmann et al. (2005) discuss likely SEDs for central accretion disks, based on observations of Type I AGNs (e.g. Walter et al., 1993, Zheng et al., 1997) and more modern theoretical models where observations are lacking. In most cases the spectrum is relatively flat in the optical-IR region, $-0.5 < \alpha_\nu < +0.3$ (where $S_\nu \propto \nu^{\alpha_\nu}$) and breaks sharply down shortwards of the Lyman edge ($\lambda_{peak} \sim 0.1\mu$m i.e. $\nu_{peak} \sim 3\ 10^{15}$ Hz) With this value of ν_{peak} and the bolometric luminosity we find $S_\nu(peak) \sim 2$ Jy. The relatively flat spectrum thus inferred between ν_{peak} and 2.2 μm is consistent with the acceptable range of α_ν.

We conclude, therefore, that the fluxes and limits measured with the VLTI at 2 and 8 μm are consistent with an accretion disk spectrum. In fact, if the emission spectrum of the accretion disk and the (relatively low) foreground extinction value are correct we *expect* to see the accretion disk in the K-band measurements. [1]

[1]This is at variance with Hönig et al. (2008), who on the basis of a simple theoretical $\nu^{1/3}$ accretion

3.5.6.2 Dust Cloud Emission

Several authors (Nenkova et al., 2002, Hönig 2006, Dullemond et al 2005) have proposed that AGN dust tori are clumped and Hönig (2008) suggest that the small component of the VINCI observations is a warm dust cloud or compact cluster of such clouds. To evaluate this suggestion in the light of our observations requires an additional assumption about the K-band extinction. If, as above, we assume the clouds to be near the nucleus this would to be of order $\gtrsim 3$ mag, the intrinsic K-band flux is $\gtrsim 1$ Jy and the 8μm $\rightarrow 2.2\mu$m spectral index is $\alpha_\nu \lesssim -0.2$. For black-body emission this implies a color temperature $T_{color} > 1300$ K, which is rather warm for dust, but not excluded, particularly if the dust is more refractory than standard silicates. If, in fact, the dust clouds are in the immediate vicinity of the nucleus, i.e. $r < 2.5$ mas, their equilibrium temperature derived from the above luminosity would be much higher than this, making dust emission very unlikely. However, as discussed at the beginning of this section, there is no direct evidence that the emission feature is physically so close to the nucleus. If the unresolved K-band source is *not* centered on the nucleus but above the main body of dust clouds, or seen through a hole in these clouds, then its intrinsic K-band flux could be as low as the observed 50 mJy, in which case the N-band upper limit provides no useful information on its properties.

Thus we conclude that the K- and N- band interferometric data can be straightforwardly be explained as emission from a hot central accretion disk if reasonable assumptions are made on the foreground emission and the accretion disk spectrum. The data can also be explained as emission from a group of hot dust clouds, but then it is unlikely that these clouds are centered around the central source. Additionally in this case, the extinction towards the core must be sufficient (i.e. $\tau_K >> 3$) to suppress the expected K-band emission from the nuclear accretion disk below the observed 50 mJy level.

3.6 Conclusions

In this paper we present interferometric observations of the nucleus of NGC 1068, using MIDI at the VLT. Extensive *uv* coverage of sixteen baselines with a maximal resolution of 7 mas has allowed us to analyse the mid-infrared (8-13μm) emission from the obscuring torus in great detail. We find the measurements consistent with emission from a compact (0.45×1.35 pc) component with a Gaussian flux distribution that is composed of hot (∼800K) silicate dust with an unusual absorption profile, which we identify as a funnel of hot dust associated with the obscuring torus. The emission is colinear, and likely co-spatial, with the well studied H_2O megamaser disk, and therefore tilted by $45°$ with respect to the radio jet. A second, more extended (3×4 pc) component of warm (∼300K) silicate dust is weakly detected, which we identify as 'body' of the torus. This second component is mostly over-resolved and its properties are not well constrained. We discuss the physical origin of the emission with respect to the torus, the masers, the ionization cone, and the radio jet. A direct image of the source at 8 μm, obtained with maximum entropy image reconstruction, is presented as well.

disk spectrum peaking at $\nu \sim 10^{17}$ Hz, for which little observational evidence exists, argued for an undetectably low accretion disk flux at $\lambda > 1\mu$m.

Since the obscuring torus is a crucial component in the accepted picture of an AGN, resolving the structure of the torus illuminates many aspects of the AGN picture. We show that in many aspects the nucleus of NGC 1068 is irregular: the orientation of the dust is tilted with respect to the jet; the PA of the visible ionization cone does not match the PA of the inner dust funnel; and the chemical composition of the dust in the torus is different than dust observed in the Milky Way.

Acknowledgements

This research was supported by the Netherlands Organisation of Scientific Research (NWO) through grant 614.000.414. Based on observations collected at the European Southern Observatory, Chile, program numbers 076.B-0743, 277.B-5014(B).
The authors would like to thank the anonymous referee, Julian Krolik, Leonard Burtscher and Demerese Salter for their helpful comments.

References

Antonucci R., 1993, Ann. Rev. Astron. & Astrophys., 31, 473
Antonucci R. R. J., Miller J. S., 1985, Astrophys. J., 297, 621
Bock J. J., Neugebauer G., Matthews K., Soifer B. T., Becklin E. E., Ressler M., Marsh K., Werner M. W., Egami E., Blandford R., 2000, Astron. J., 120, 2904
Capetti A., Axon D. J., Macchetto F. D., Marconi A., Winge C., 1999, Astrophys. J., 516, 187
Claussen M. J., Lo K.-Y., 1986, Astrophys. J., 308, 592
Cohen M., Walker R. G., Carter B., Hammersley P., Kidger M., Noguchi K., 1999, Astron. J., 117, 1864
Das V., Crenshaw D. M., Kraemer S. B., Deo R. P., 2006, Astron. J., 132, 620
Dullemond C. P., van Bemmel I. M., 2005, Astron. & Astrophys., 436, 47
Evans I. N., Ford H. C., Kinney A. L., Antonucci R. R. J., Armus L., Caganoff S., 1991, Astrophys. J., 369, L27
Galliano E., Alloin D., Granato G. L., Villar-Martín M., 2003, Astron. & Astrophys., 412, 615
Galliano E., Pantin E., Alloin D., Lagage P. O., 2005, Mon. Not. R. Astron. Soc., 363, L1
Gallimore J. F., Baum S. A., O'Dea C. P., 2004, Astrophys. J., 613, 794
Gallimore J. F., Henkel C., Baum S. A., Glass I. S., Claussen M. J., Prieto M. A., Von Kap-herr A., 2001, Astrophys. J., 556, 694
Garcia-Lorenzo B., Mediavilla E., Arribas S., del Burgo C., 1997, Astrophys. J., 483, L99+
Greenhill L. J., 1998, in Zensus J. A., Taylor G. B., Wrobel J. M., eds, IAU Colloq. 164: Radio Emission from Galactic and Extragalactic Compact Sources Vol. 144 of Astronomical Society of the Pacific Conference Series, Water in NGC 1068. pp 221–+
Greenhill L. J., Booth R. S., Ellingsen S. P., Herrnstein J. R., Jauncey D. L., McCulloch P. M., Moran J. M., Norris R. P., Reynolds J. E., Tzioumis A. K., 2003, Astrophys. J., 590, 162
Hönig S. F., Beckert T., Ohnaka K., Weigelt G., 2006, Astron. & Astrophys., 452, 459
Hönig S. F., Beckert T., Ohnaka K., Weigelt G., 2007, in Ho L. C., Wang J.-W., eds, The Central Engine of Active Galactic Nuclei Vol. 373 of Astronomical Society of the Pacific Conference Series, 3D Radiative Transfer Modeling of Clumpy Dust Tori Around AGN. pp 487–+
Hönig S. F., Prieto M. A., Beckert T., 2008, Astron. & Astrophys., 485, 33
Huré J.-M., 2002, Astron. & Astrophys., 395, L21
Jaffe W., Meisenheimer K., Röttgering H. J. A., Leinert C., Richichi A., Chesneau O., Fraix-Burnet D., Glazenborg-Kluttig A., Granato G.-L., Graser U., Heijligers B., Köhler R., Malbet F., Miley G. K., Paresce F., Pel J.-W., Perrin G., Przygodda F., Schoeller M., Sol H., Waters L. B. F. M., Weigelt G., Woillez J., de Zeeuw P. T., 2004, Nature, 429, 47
Jaffe W. J., 2004, in Traub W. A., ed., New Frontiers in Stellar Interferometry, Proceedings of SPIE p.715 Vol. 5491
Kartje J. F., Königl A., 1996, Vistas in Astronomy, 40, 133
Kemper F., Vriend W. J., Tielens A. G. G. M., 2004, Astrophys. J., 609, 826
Kinney A. L., Schmitt H. R., Clarke C. J., Pringle J. E., Ulvestad J. S., Antonucci R. R. J., 2000, Astrophys. J., 537, 152
Krolik J. H., Begelman M. C., 1988, Astrophys. J., 329, 702
Kumar P., 1999, Astrophys. J., 519, 599
Leinert C., Graser U., Przygodda F., and 21 others *Astronomy & Space Science*, 286, 73
Lodato G., Bertin G., 2003, Astron. & Astrophys., 398, 517
Mason R. E., Geballe T. R., Packham C., Levenson N. A., Elitzur M., Fisher R. S., Perlman E., 2006, Astrophys. J., 640, 612
Nenkova M., Ivezić Ž., Elitzur M., 2002, Astrophys. J., 570, L9
Neufeld D. A., Maloney P. R., Conger S., 1994, Astrophys. J., 436, L127+
Oliva E., Marconi A., Cimatti A., Alighieri S. D. S., 1998, Astron. & Astrophys., 329, L21
Oliva E., Salvati M., Moorwood A. F. M., Marconi A., 1994, Astron. & Astrophys., 288, 457
Osterbrock D. E., Shaw R. A., 1988, Astrophys. J., 327, 89
Poncelet A., Doucet C., Perrin G., Sol H., Lagage P. O., 2007, Astron. & Astrophys., 472, 823
Poncelet A., Perrin G., Sol H., 2006, Astron. & Astrophys., 450, 483
Rhee J. H., Larkin J. E., 2006, Astrophys. J., 640, 625
Poncelet, A., Sol, H. , Perrin, G., 2008, Astron. & Astrophys., 481, 305

Sanders D. B., Phinney E. S., Neugebauer G., Soifer B. T., Matthews K., 1989, Astrophys. J., 347, 29
Schartmann M., Meisenheimer K., Camenzind M., Wolf S., Henning T., 2005, Astron. & Astrophys., 437, 861
Schartmann M., Meisenheimer K., Camenzind M., Wolf S., Tristram K. R. W., Henning T., 2008, Astron. & Astrophys., 482, 67
Speck A. K., Barlow M. J., Sylvester R. J., Hofmeister A. M., 2000, Astron. & Astrophys. Supp. Series, 146, 437
Sturm E., Lutz D., Tran D., Feuchtgruber H., Genzel R., Kunze D., Moorwood A. F. M., Thornley M. D., 2000, Astron. & Astrophys., 358, 481
Thatte N., Quirrenbach A., Genzel R., Maiolino R., Tecza M., 1997, Astrophys. J., 490, 238
Tomono D., Doi Y., Usuda T., Nishimura T., 2001, Astrophys. J., 557, 637
Tristram K. R. W., Meisenheimer K., Jaffe W., Schartmann M., Rix H.-W., Leinert C., Morel S., Wittkowski M., Röttgering H., Perrin G., Lopez B., Raban D., Cotton W. D., Graser U., Paresce F., Henning T., 2007, Astron. & Astrophys., 474, 837
Urry C. M., Padovani P., 1995, Pub. Astron. Soc. Pacific, 107, 803
Veilleux S., Bland-Hawthorn J., 1997, Astrophys. J., 479, L105+
Walter R., Fink H. H., 1993, Astron. & Astrophys., 274, 105
Weigelt G., Wittkowski M., Balega Y. Y., Beckert T., Duschl W. J., Hofmann K.-H., Men'shchikov A. B., Schertl D., 2004, Astron. & Astrophys., 425, 77
Weingartner J. C., Draine B. T., 2001, Astrophys. J., 548, 296
Wittkowski M., Kervella P., Arsenault R., Paresce F., Beckert T., Weigelt G., 2004, Astron. & Astrophys., 418, L39
Zheng W., Kriss G. A., Telfer R. C., Grimes J. P., Davidsen A. F., 1997, Astrophys. J., 475, 469